nature energy

Article

https://doi.org/10.1038/s41560-024-01569-9

Design principles for enabling an anode-free sodium all-solid-state battery

Received: 1 November 2023

Accepted: 4 June 2024

Published online: 03 July 2024

Check for updates

Grayson Deysher[1], Jin An Sam Oh[2], Yu-Ting Chen[1], Baharak Sayahpour[1], So-Yeon Ham[1], Diyi Cheng[1], Phillip Ridley[2], Ashley Cronk[1], Sharon Wan-Hsuan Lin[2], Kun Qian[2], Long Hoang Bao Nguyen[2], Jihyun Jang[2,3] ✉ & Ying Shirley Meng[2,4] ✉

Anode-free batteries possess the optimal cell architecture due to their reduced weight, volume and cost. However, their implementation has been limited by unstable anode morphological changes and anode–liquid electrolyte interface reactions. Here we show that an electrochemically stable solid electrolyte and the application of stack pressure can solve these issues by enabling the deposition of dense sodium metal. Furthermore, an aluminium current collector is found to achieve intimate solid–solid contact with the solid electrolyte, which allows highly reversible sodium plating and stripping at both high areal capacities and current densities, previously unobtainable with conventional aluminium foil. A sodium anode-free all-solid-state battery full cell is demonstrated with stable cycling for several hundred cycles. This cell architecture serves as a future direction for other battery chemistries to enable low-cost, high-energy-density and fast-charging batteries.

Recent years have shown an increasing demand for electric vehicles and energy storage devices for large-scale grid applications. Batteries are critical for enabling these technologies, and although they have improved substantially since the introduction of the first commercial lithium-ion battery in 1990[1], further enhancements are needed to enable higher energy density and lower-cost energy storage systems. Commonly used lithium is geographically concentrated and has experienced a rapid increase in price as the demand for batteries grows[2]. Sodium-based materials, on the other hand, are much less expensive and more widely available. Whereas sodium batteries are often assumed to sacrifice energy density in favour of lower cost, in this work we show that lower-cost sodium batteries may still achieve a high energy density comparable to current lithium systems due to the natural advantages of several sodium materials compared with their lithium counterparts.

To compete with the high energy density possessed by lithium-ion batteries, a considerable change in sodium battery architectures is needed. A recently popularized idea is the use of an anode-free cell design[3]. Unlike conventional batteries, anode-free batteries are those in which no anode active material is used. Rather than using carbon- or alloy-based anode materials to store ions during cell charging, anode-free batteries rely on the electrochemical deposition of alkali metal directly onto the surface of a current collector (Fig. 1a). This achieves the lowest possible reduction potential, thus enabling higher cell voltage, lowers the cell cost and increases energy density due to the removal of the anode active material (Fig. 1b).

However, many challenges have prevented the use of an anode-free architecture for both lithium and sodium chemistries. The deposition of lithium/sodium metal in conventional organic liquid electrolyte batteries is known to produce a porous or mossy-like morphology[4,5]. Additionally, liquid electrolytes commonly react with the deposited metal forming a solid–electrolyte interphase (SEI)[6–9]. Continuous anode morphological changes during cycling inevitably result in the continuous formation of SEI, which steadily consumes the active material inventory[10]. Although several strategies have been explored including modifications to the liquid electrolyte[3,11–13], current collector[14], cell stack pressure[15] and cycling protocol[16], they have yielded only moderate improvements with many demonstrating only tens of cycles and/or low initial Coulombic efficiencies (ICE). Instead, a better approach is

[1]Program of Materials Science and Engineering, University of California San Diego, La Jolla, CA, USA. [2]Department of NanoEngineering, University of California San Diego, La Jolla, CA, USA. [3]Department of Chemistry, Sogang University, Seoul, Republic of Korea. [4]Pritzker School of Molecular Engineering, The University of Chicago, Chicago, IL, USA. ✉e-mail: jihyunjang@sogang.ac.kr; shirleymeng@uchicago.edu

https://doi.org/10.1038/s41560-024-01569-9

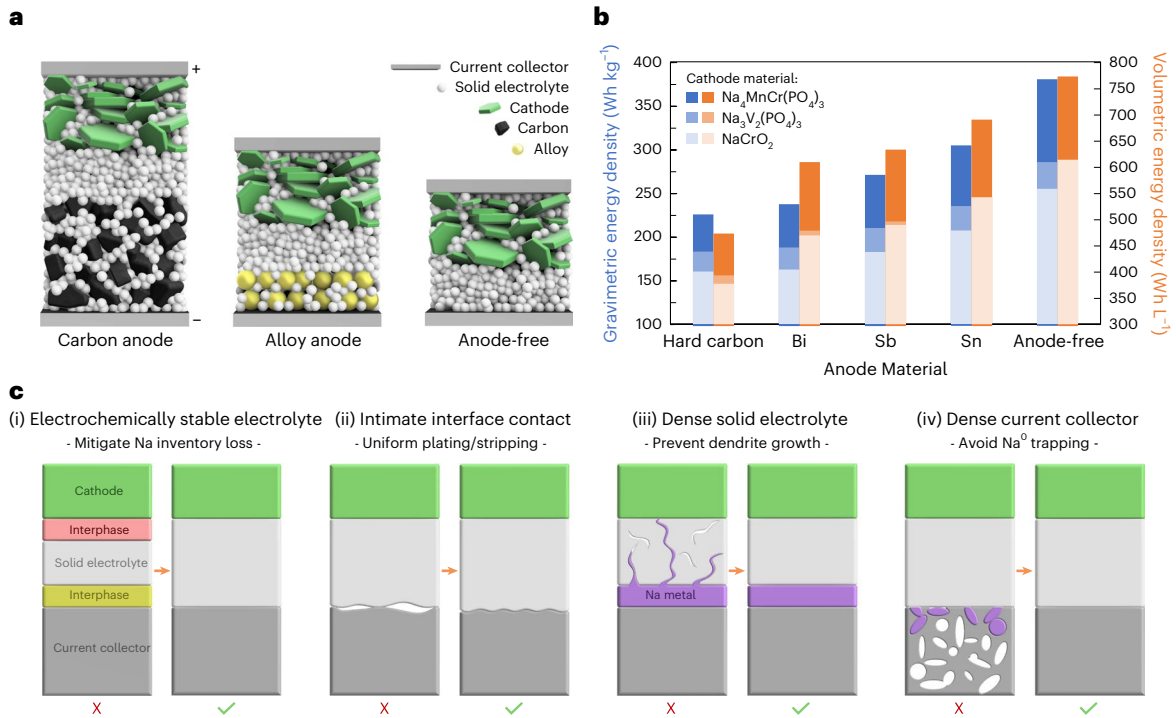

Fig. 1 | Anode-free schematics and energy density calculations. a, Cell schematic for carbon anodes, alloy anodes and an anode-free configuration. **b**, Theoretical energy density comparison for various sodium anode materials. Values used for the calculations can be found in Supplementary Table 1. **c**, Schematic illustrating the four requirements for enabling an anode-free all-solid-state battery. These include an electrochemically stable electrolyte (i), intimate interface contact (ii), a dense solid electrolyte (iii) and a dense current collector (iv).

to utilize solid-state electrolytes. Due to their solid nature, the solid electrolyte separator layer is limited to a planar two-dimensional contact area with the negative electrode current collector (Fig. 1a). This can facilitate less solid–electrolyte interfacial reactions compared with large surface area three-dimensional anodes in liquid electrolyte systems. Furthermore, the use of applied stack pressure can enable a dense metal anode, which is required for mitigating contact loss, void formation and cell short circuiting[17].

A few works have demonstrated a solid-state concept in lithium anode-free thin film batteries[18,19]; however these cell formats have limited areal capacities due to the thin cathode layers. Several recent works have attempted to enable anode-free cycling in bulk lithium solid-state cells using oxide-[20] or sulfide-based[21] solid electrolytes, however these cells also have exhibited poor reversibility. Several strategies have been explored for solving this challenge such as modifying the current collector[21], adding sacrificial lithium sources[22,23] or incorporating lithiophilic alloying compounds such as silver[24,25]. However, these strategies either fail to enable sufficiently reversible cycling or add inactive material to the cell, which reduces the advantage of utilizing an anode-free design. To the best of our knowledge, only one recent attempt at making a sodium anode-free solid-state battery has been reported, although no electrochemical cycling was demonstrated[26]. Therefore, it is critical to first determine the critical factors governing the performance of anode-free solid-state batteries.

To enable an anode-free sodium solid-state battery, four conditions must be met (Fig. 1c). First, an electrochemically stable or highly passivating electrolyte is needed to avoid the consumption of active sodium inventory due to the formation of a SEI layer. Second, intimate and robust solid–solid interface contact between the solid electrolyte and the current collector is needed for repeated sodium plating/stripping. Any void between the materials will prevent electron transfer, and Na^0 deposition cannot occur. Third, a dense solid-state electrolyte separator is needed. It is known that pores, cracks and imperfections can promote the growth of metal filaments through the separator resulting in cell short circuiting[27–31]. Fourth, the current collector needs to be highly dense. Whereas porous current collectors have been shown to be effective in liquid electrolyte cells due to their higher surface area and lowered local current densities[32,33], these current collectors cannot be used in solid-state cells. Unlike liquid electrolytes, solid-state electrolytes cannot flow into the pores of the current collector, therefore sodium plated inside the pores will become trapped due to the lack of sodium conduction pathways during stripping.

In this work, we seek to meet these four requirements to enable an anode-free sodium all-solid-state battery. An electrochemically stable sodium borohydride solid electrolyte was found to achieve near-perfect contact with a pelletized aluminium current collector. Morphological evaluation found that the borohydride electrolyte can achieve a nearly fully dense structure by cold pressing, which inhibited the penetration of sodium dendrites and enabled cycling at current densities exceeding 6 mA cm^{-2}. Additionally, the aluminium current collector was also found to be highly dense thus meeting the four requirements outlined above. As a proof of concept, an anode-free sodium all-solid-state battery with $NaCrO_2$ as the cathode, under 10 MPa stack pressure at 40 °C, was cycled for 400 cycles with an average Coulombic efficiency of 99.96%. This work strives to be framework for the future development of sodium and other battery chemistries with high energy densities and offers a description of the critical factors governing their electrochemical performance.

Electrochemically stable electrolyte

An anode-free half cell was assembled with the commonly used Na_3PS_4 (NPS) solid electrolyte paired with an aluminium foil current collector and Na_9Sn_4 counter electrode (Supplementary Fig. 1). The ICE was 4%. This can be attributed to the reduction of NPS at low potential forming Na_3P[34], which is a known mixed conductor, leading to continuous SEI growth and the irreversible consumption of sodium inventory. To solve

https://doi.org/10.1038/s41560-024-01569-9

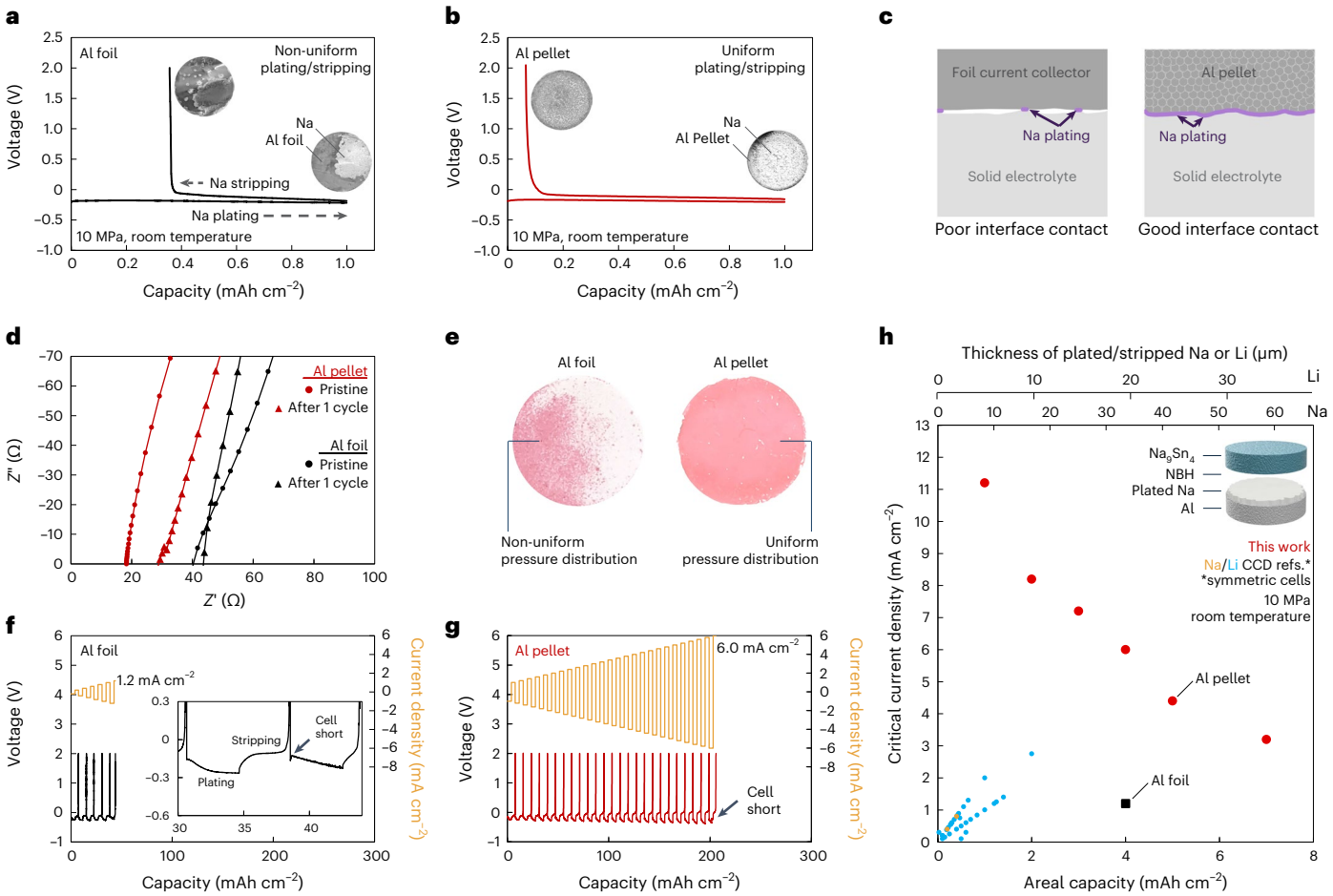

Fig. 2 | Al pellet comparison with Al foil. a,**b**, Plating/stripping behaviour at 1 mA cm^{-2} current density for Al foil (**a**) and Al Pellet current collectors (**b**). **c**, Schematic illustrating the ability of aluminium powder to form intimate contact with the solid electrolyte layer. **d**, Impedance measurements before and after cycling Al foil and Al pellet cells. Real impedance is denoted Z' and imaginary impedance is denoted Z''. **e**, Pressure paper showing the distribution of pressure over the cell area when using Al foil and Al pellet current collectors. **f**,**g**, Critical current density when cycling 4 mAh cm^{-2} capacity with Al foil with inset showing fine details of the voltage profile during cell failure (**f**) and Al pellet current collectors (**g**). **h**, Critical current density (CCD) evaluation as a function of areal capacity at room temperature when using an Al pellet current collector. Full voltage profile data for these tests can be found in Supplementary Fig. 5. Literature data that utilized cold-pressed solid electrolytes are added for comparison[56–78]. All cycling data in this figure were obtained at room temperature under 10 MPa stack pressure.

the electrochemical instability, a sodium borohydride solid electrolyte ($Na_4B_{10}H_{10}B_{12}H_{12}$ (NBH)) was used as the separator (Supplementary Fig. 2). NBH has previously been shown to be electrochemically stable against sodium metal[34,35]. Sodium was again electrochemically plated onto the aluminium foil and then stripped away, resulting in a higher ICE of 64% (Fig. 2a). This demonstrates the importance of using an electrochemically stable solid electrolyte in anode-free cells. However, the efficiency when using NBH remained unacceptably low; therefore other aspects of the anode-free architecture require improvement.

Intimate interface contact

Metal foils are by far the most common current collectors used in batteries, however only a small area of the foil was plated with sodium (Fig. 2a), which was confirmed to be metallic sodium by X-ray diffraction (XRD) (Supplementary Fig. 3). This indicates that there is not sufficient solid–solid contact between the solid electrolyte and the aluminium foil current collector as sodium can only deposit where there is a connection between the incoming Na^+ from the solid-state electrolyte and the electron from the current collector. After stripping, sodium was still observed on the foil, thus explaining the relatively low ICE (Fig. 2a). This can be attributed to poor interface contact among the solid electrolyte, sodium metal and foil current collector, which resulted in incomplete stripping of the sodium. This indicates that conventional aluminium foil does not meet the intimate interface contact requirement, resulting in poor reversibility.

To improve the solid–solid interfacial contact between the solid electrolyte and current collector, pelletized aluminium was pressed onto the solid electrolyte separator during cell fabrication in the same process as when using aluminium foil (Fig. 2b). Aluminium powder can easily conform to the variable topography of the solid electrolyte separator layer, which is formed during the cell fabrication process (Fig. 2c). This current collector will be referred to as aluminium pellet. When cycled under the same conditions, the half cell ICE was greatly improved to 93%. Additionally, a variety of aluminium particle sizes were evaluated and exhibited similar ICE values (Supplementary Fig. 4).

When cells were disassembled after plating and after one full cycle, the uniformity of the sodium metal distribution on the current collector surface was found to be greatly improved. Even after plating 1 mAh cm^{-2}, which theoretically amounts to an 8.8 μm Na metal layer, the deposition was already uniformly distributed. This implies that the aluminium powder can form a more uniform and intimate contact with the solid electrolyte separator across the entire cell area compared with traditional aluminium foil. This was further demonstrated with electrochemical impedance spectroscopy, which showed a lower

https://doi.org/10.1038/s41560-024-01569-9

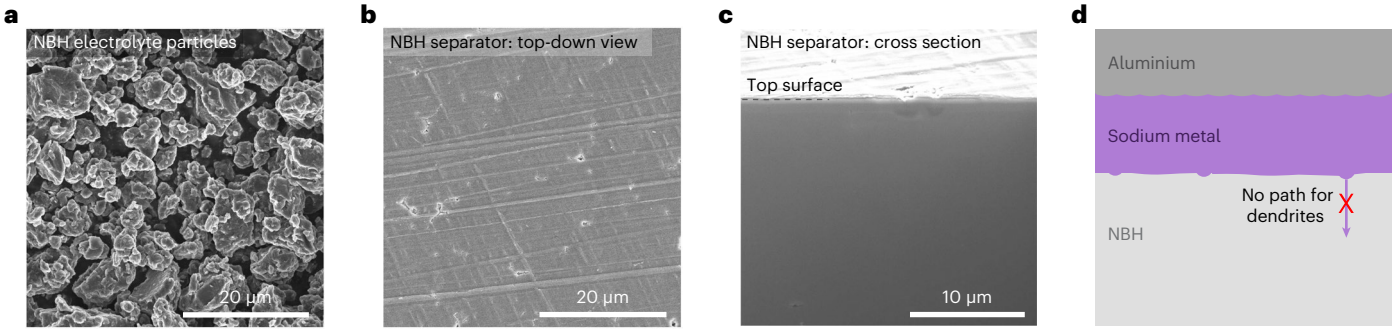

Fig. 3 | Evaluation of NBH morphology. a,**b**, SEM of NBH particles (**a**) and top view of the NBH separator after cold pressing (**b**). **c**, FIB-SEM cross section view of NBH separator. **d**, Schematic illustrating the propensity of sodium to deposit without forming dendrites through the electrolyte.

interfacial resistance when using the aluminium pellet current collector (Fig. 2d). Furthermore, the aluminium pellet was shown to evenly distribute the applied stack pressure across the entire area of the cell, which was found by inserting pressure-sensitive paper in between the current collector and solid electrolyte layers during cell fabrication (Fig. 2e). This probably also helps in uniformly spreading the soft sodium metal as it is plated in cells under stack pressures (10 MPa stack pressure used for this study) well above the yield strength of sodium (~0.2 MPa) (ref. 36).

Due to the improved contact and sodium plating uniformity, the applied current will be distributed over a larger area compared with when using aluminium foil. As high current density promotes the formation of dendrites[37–39], which can lead to cell short circuiting, lowering the local current density enables cell cycling at higher total currents. When using aluminium foil and cycling with 4 mAh cm^{-2} capacity between the electrodes, the critical current density was found to be 1.2 mA cm^{-2} (Fig. 2f). The cell failed during the sodium plating step, and the Na_9Sn_4 counter electrode was found to cycle at much higher currents (Supplementary Fig. 6); therefore this critical current density can be attributed to failure by sodium dendrite penetration through the electrolyte during plating. When using the aluminium pellet current collector, the critical current density increased to 6.0 mA cm^{-2} (Fig. 2g). Interestingly, compared with previously reported critical current density values for cold-pressed cells (Fig. 2h), our data show successful cycling at much higher currents, even when using an aluminium foil current collector. Most previously reported critical current density values are ≤2 mA cm^{-2} at ≤2 mAh cm^{-2} capacity. This indicates that there may be another factor governing the high current ability of these cells, besides the type of current collector.

Dense solid electrolyte

Anode-free cells rely on the nature of the interface between the current collector and the solid electrolyte. Therefore, the solid electrolyte properties are also important to consider when assessing this type of cell architecture. Focused-ion beam milling scanning electron microscopy (FIB-SEM) was used to evaluate the morphology of the NBH solid electrolyte after cold pressing to form the separator layer (Fig. 3a–c). The NBH electrolyte separator exhibited an extremely dense morphology. The crosshatch line pattern textured on the surface is due to the imperfect titanium plunger used to press the solid electrolyte layer (Supplementary Fig. 7). More importantly, only a few rounded micron-sized surface pores were observed, indicating good compaction without the need for high temperature sintering (Fig. 3b). The cross section of the NBH was intentionally milled at the spot of one of the surface pores to examine how deep they protrude into the electrolyte layer. It was found that the pores have a rounded morphology that does not extend further than ~1 µm (Fig. 3c). In addition to the intimate interface contact achieved by using the aluminium pellet current collector, the dense morphology of NBH also contributes to the observed high critical current densities. It is known that imperfections in the solid electrolyte separator such as pores and cracks can result in dendrite penetration and cell short circuiting[27–31]. Without these imperfections, it becomes much more difficult for sodium to penetrate the solid electrolyte layer (Fig. 3d).

To compare with lithium solid electrolytes, $Li_4B_{10}H_{10}B_{12}H_{12}$ (LBH) was selected as a direct comparison with NBH as it has also been shown to achieve an electrochemically stable interface with lithium metal[40]. Li_6PS_5Cl (LPSCl) was also selected due to its common use in lithium solid-state batteries. These solid electrolytes were found to exhibit porous morphologies after cold pressing (Supplementary Fig. 8). When these electrolytes were used as the separator in lithium half cells, the cells short circuited shortly after the plating step began and could only be successfully cycled at much lower current densities (0.1 mA cm^{-2}). This can be attributed to the soft lithium creeping into the surface cracks of the separators[30], which can result in current concentrations at the tips of the lithium metal filaments and further exacerbate the filament growth through the solid electrolyte[41]. NBH materials on the other hand have been shown to be softer than their lithium counterparts[42], but previously there have been no visual observations of the highly dense morphology that can be achieved by cold pressing when using NBH. The high sodium critical current density can be attributed to this newly revealed ability of this borohydride electrolyte.

Dense current collector

To probe the effect of the current collector morphology, aluminium, copper and titanium were selected for comparison due to their common use in solid-state battery research as current collectors and cell materials. Like aluminium, copper and titanium do not form alloys with sodium, ensuring that they will only act as a current collector[43–45]. Using a half cell configuration, the plate/strip ICEs were noticeably different (Fig. 4a–c). There were also small slope regions observed in the voltage curves during the initial stages of plating when using copper and titanium. This is attributed to the surface oxide layers present on these metals that react with the incoming sodium forming an oxide (Supplementary Fig. 9). This probably contributes partially to the irreversible capacity due to the high bonding energy between sodium and oxygen although the thin nature of the surface oxides and the small capacity observed within the slope regions indicates that it is not the major factor affecting the overall irreversibility.

After repeated cycling the aluminium cells exhibited the highest capacity retention followed by copper and then titanium, which had the lowest capacity retention (Fig. 4d). As the solid electrolyte–current collector interface is known to play a critical role in the cyclability of solid-state anode-free cells (Fig. 2), the surface topographies of the three current collectors were compared using optical profilometry (Fig. 4e–g). Whereas all three current collectors exhibited slightly

https://doi.org/10.1038/s41560-024-01569-9

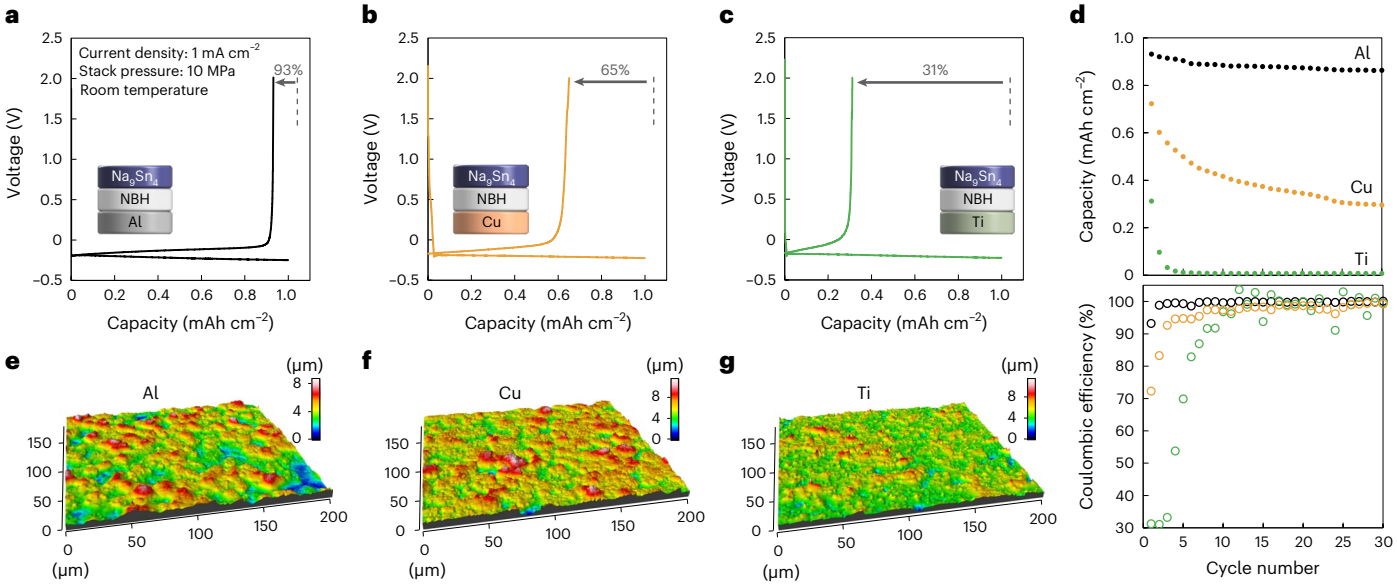

Fig. 4 | Evaluation of various pelletized current collectors. a–c, First cycle plating/stripping voltage curves of half cells using Al (**a**), Cu (**b**) and Ti (**c**) pellet current collectors. **d**, Electrochemical performance of the same three cells over 30 cycles. **e–g**, Optical profilometry measurements of the surface topography of Al (**e**), Cu (**f**) and Ti (**g**) pellet current collectors. All cycling data in this figure were obtained at room temperature under 10 MPa stack pressure with a current density of 1 mA cm^{-2}.

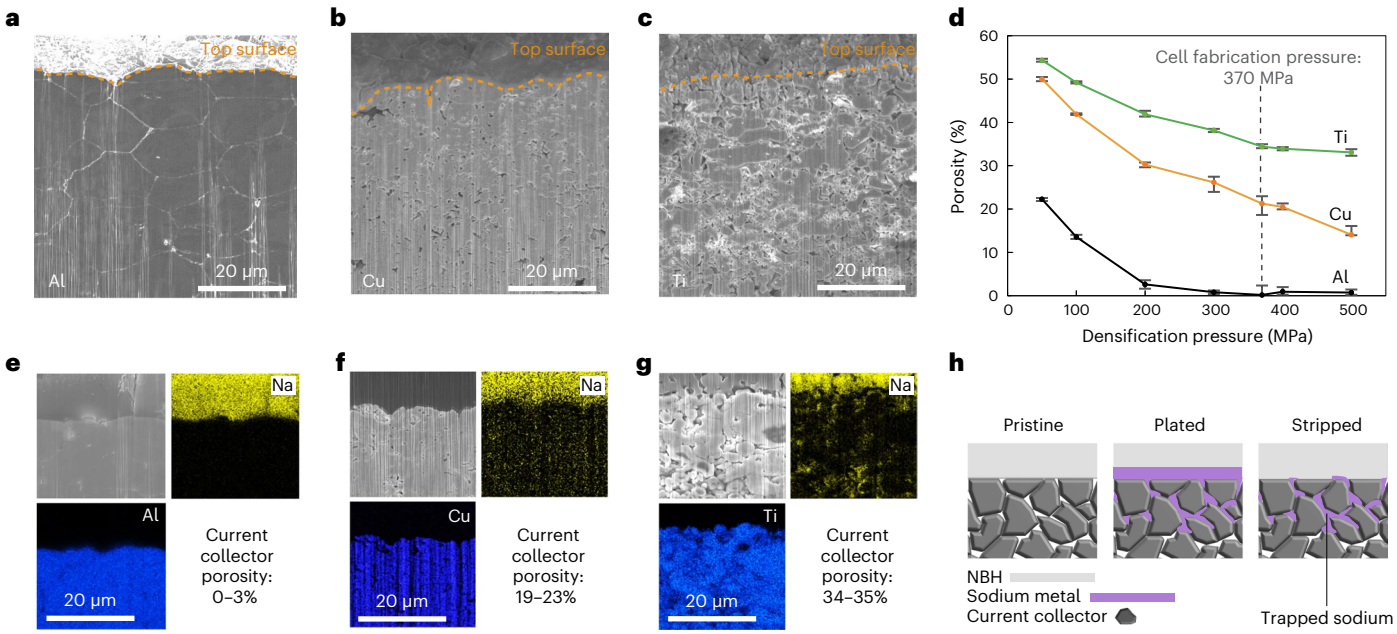

Fig. 5 | Evaluation of pelletized current collector morphologies. a–c, FIB-SEM cross section views of pristine Al (**a**), Cu (**b**) and Ti (**c**) pellet current collectors. **d**, Current collector porosity as a function of fabrication pressure. Data are presented as mean values with error bars representing the minimum and maximum values measured from a set of three thickness measurements across the length of each sample. **e–g**, FIB-SEM cross section views of Al (**e**), Cu (**f**) and Ti (**g**) current collectors after one plate/strip cycle with EDS mapping. **h**, Schematic of Na trapping mechanism for porous current collectors.

different surface textures, probably correlated to their powder morphology (Supplementary Fig. 10), the roughness of their surfaces were close in value; 0.98 μm, 1.05 μm and 0.90 μm for aluminium, copper and titanium, respectively. Therefore, their degree of contact with the solid electrolyte separator should be similar. This indicates that the reversibility differences may be due to a bulk current collector effect rather than an interface variation.

To evaluate the bulk morphology of the three current collectors, FIB-SEM was used to image their cross sections. As shown in Fig. 5a–c, the aluminium current collector was almost fully dense. By using the weight and volume of the pellet, the porosity of the aluminium was calculated to be 0–3%. In contrast, the copper current collector contained many micron-sized pores (19–23% porosity) and, similarly, the titanium current collector contained many larger pores (34–35% porosity). To establish a quantitative trend comparison between these three materials, several current collectors were fabricated at various pressures, and their porosities were determined (Fig. 5d). It was found that aluminium powder can densify more easily than copper and

https://doi.org/10.1038/s41560-024-01569-9

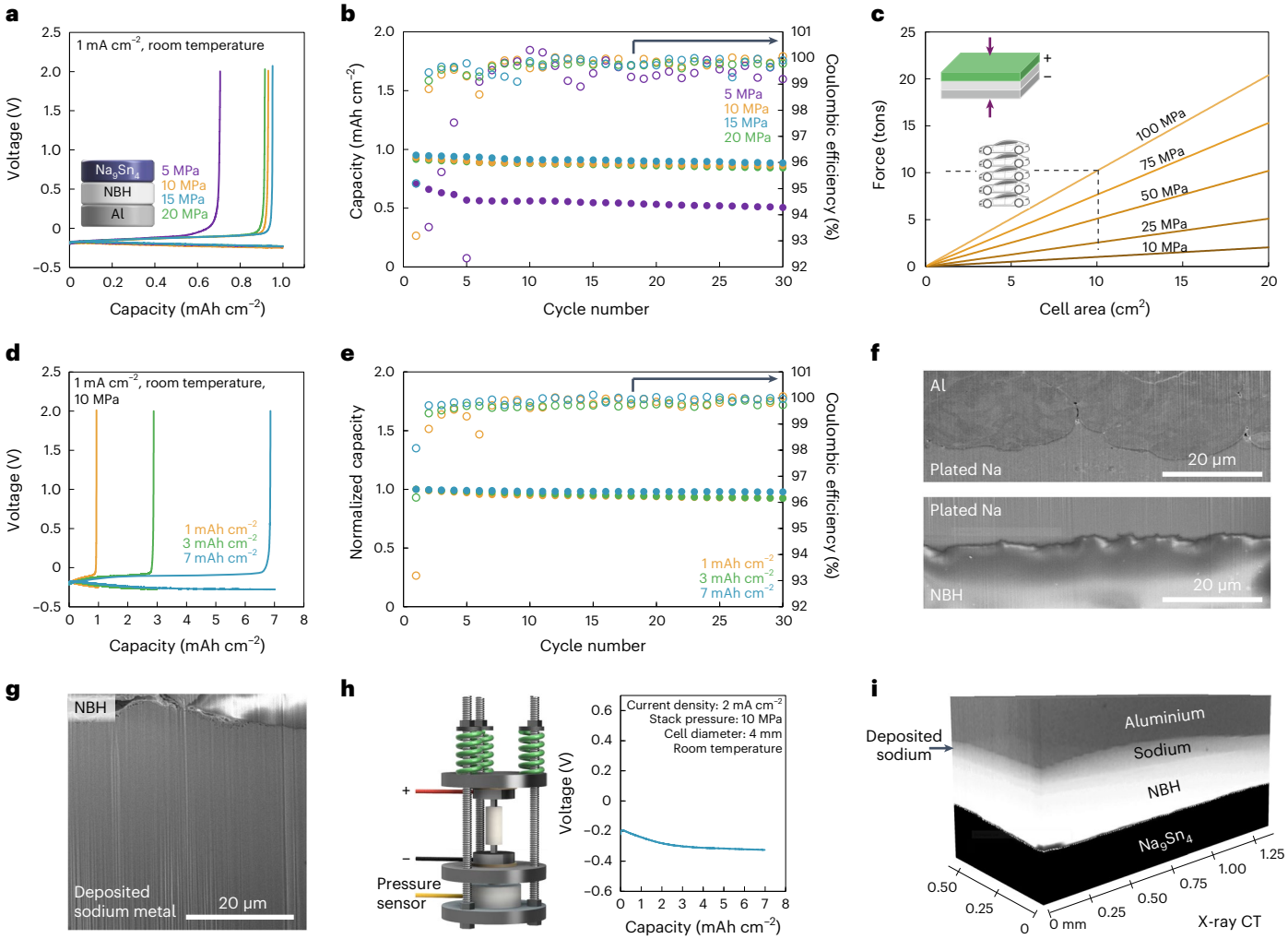

Fig. 6 | Effects of cell stack pressure and areal capacity. a, Voltage profiles for Na_9Sn_4|NBH|Al half cells cycled at 5, 10, 15 and 20 MPa. **b**, Capacity retention during extended cycling of the same cells. **c**, Force required to achieve various stack pressures. **d**, Voltage profiles for Na_9Sn_4|NBH|Al half cells cycled with 1, 3 and 7 mAh cm^{-2} capacities. **e**, Capacity retention during extended cycling of the same cells. **f**,**g**, Cryo-FIB/SEM images of the Na–Al and Na–NBH interfaces (**f**) and thick plated sodium (**g**). **h**, Cell holder schematic and cycling data for a custom 4 mm diameter X-ray computed tomography cell. **i**, X-ray computed tomography scan of 7 mAh cm^{-2} plated sodium metal. All cycling data in this figure were obtained at room temperature.

titanium powders, which can be explained by the varying mechanical properties of these three materials in which aluminium possesses the lowest Vickers hardness (~160 MPa) compared with copper (~370 MPa) and titanium (~970 MPa)[46].

To evaluate the potential impact of the current collector porosity on the reversibility of sodium plating/stripping, FIB-SEM was used again on cycled cells after one plate/strip cycle. These results (Fig. 5e–g) show that when pores are present in the current collector, sodium metal can become trapped inside during plating. Because there is no liquid electrolyte present, and the solid electrolyte separator is unable to flow into the current collector pores, the sodium in the pores becomes ionically insulated after the sodium metal at the solid electrolyte–current collector interface is stripped away (Fig. 5h). This results in a sodium trapping effect, which can be seen in the sodium energy dispersive X-ray spectroscopy (EDS) maps (Fig. 5e–g). Therefore, the use of aluminium was found to be critical to enable reversible plating/stripping, as it is soft enough to become highly dense after cold pressing during cell fabrication.

Stack pressure and sodium morphology

Beyond enabling reversible cycling in an anode-free architecture, there are other important practical cell performance considerations to evaluate. Often, high stack pressures (50–250 MPa) are used for solid-state cell cycling[30,47–51]. This is not a commercially viable option because larger area cells, such as 3 × 3 cm^2, can require forces exceeding 10 tonnes (Fig. 6c). It is likely that no battery pack casing will be able to achieve such high pressures safely and consistently without using a heavy construction and thus lowering the cell energy density. Instead, lower pressure cycling should become the norm for solid-state battery research. Due to their low moduli, bulk alkali metal anodes are known to work well at lower pressures[52,53]. To assess the effect of cell stack pressure on cyclability in this anode-free cell configuration, half cells were cycled at 5, 10, 15 and 20 MPa of constant stack pressure (Fig. 6a,b). When 10–20 MPa was used, the cells exhibited very similar reversibility and capacity retention. This indicates that pressures higher than 10 MPa are not needed. Five MPa cycling was found to be less reversible. As no noticeable difference in the cyclability of Na_9Sn_4 was observed at 5 and 10 MPa (Supplementary Fig. 6), the change in anode-free half cell performance at 5 MPa can be attributed to the anode-free side. The lower reversibility of anode-free cycling at 5 MPa can be attributed to the difficulty in maintaining intimate solid–solid contact between the current collector, sodium metal and solid electrolyte, which is essential for complete stripping of the deposited sodium. Currently, this is a common limitation for solid-state batteries due to the difficulty in

https://doi.org/10.1038/s41560-024-01569-9

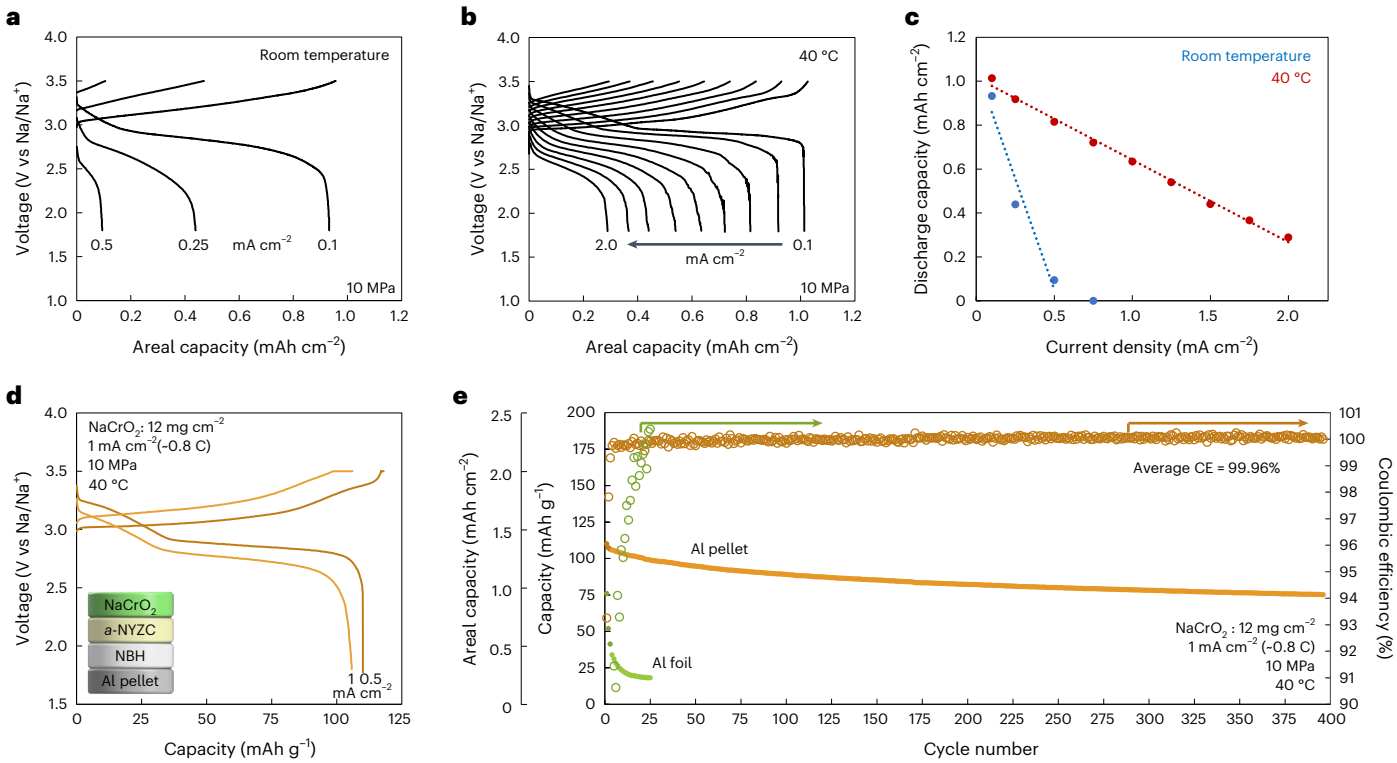

Fig. 7 | Anode-free sodium all-solid-state full cell cycling. a,**b**, Voltage curves of a sodium anode-free full cell cycled at various currents at room temperature (**a**) and 40 °C (**b**). Voltage curves for the first three formation cycles are not shown. **c**, Cathode capacity as a function of current density. **d**,**e**, Voltage curves of a sodium anode-free solid-state full cell including a constant voltage hold at 3.5 V (**d**) and cell capacity over 400 cycles for the same cell combined with Al foil data for comparison (**e**). Energy efficiency data is provided in Supplementary Fig. 18. A comparison with Na_9Sn_4 anode is included in Supplementary Fig. 19. $NaCrO_2$ cathode was used in all cells. All cycling data in this figure was obtained under 10 MPa stack pressure.

maintaining intimate contact between solid materials. Stack pressure requirements may necessitate heavier battery pack casings, which can limit the overall system energy density and increase the cost. As such, it is important for future research to focus on finding ways to lower the required stack pressure. One method may be the use of elevated temperatures. Lower pressures such as 5 and 1 MPa can be enabled using a slightly elevated cycling temperature (Supplementary Fig. 11). At 40 °C, the efficiency of 5 and 1 MPa cells became similar to that of 10 MPa presumably due to the softening of metallic sodium[54], which can facilitate the retention of intimate solid–solid interfaces even at lower pressures.

Areal capacity is also important to consider as higher areal capacities result in higher overall energy densities by maximizing the active:inactive material ratio. Using 10 MPa stack pressure, it was found that cycling 1, 3 and 7 mAh cm^{-2} capacity of sodium, corresponding to 8.8, 26.5 and 61.9 µm of deposited sodium, respectively, exhibited very similar reversibility and capacity retention (Fig. 6d–e). Furthermore, similar plating/stripping efficiencies were observed for both 10 and 13 mm diameter cells, which indicates that larger cell areas are also possible (Supplementary Fig. 12). Lastly, an anode-free half cell was found to exhibit a high Coulombic efficiency for 1,000 cycles (Supplementary Fig. 13). The sodium morphology and NBH interface conformity was evaluated using cryogenic FIB-SEM (Fig. 6f) and EDS mapping (Supplementary Fig. 14). The aluminium interface conformity was also evaluated. The sodium was found to form a dense and intimate interface with both the NBH and the Al, which is critical for enabling sufficient ion and electron transfer, respectively.

To evaluate the bulk sodium morphology after plating, a cell was examined using cryo-FIB-SEM after plating 7 mAh cm^{-2} capacity (Fig. 6g). The electrochemically deposited sodium metal contained no pores in the area examined. This dense morphology is unique to this solid-state cell architecture under stack pressure compared with the mossy sodium observed when using liquid electrolytes at very low pressures. To evaluate the sodium morphology over a larger scale, an X-ray computed tomography scan was performed on a smaller 4 mm diameter cell after plating 7 mAh cm^{-2} capacity (Fig. 6h). The sodium was found to be uniformly distributed across the surface of the current collector (Fig. 6i) and no discernable morphological features were observed. This can be attributed to the homogeneous plating of sodium due to the intimate and electrochemically stable interface, which is responsible for enabling the highly efficient plating/stripping observed for areal capacities as high as 7 mAh cm^{-2}.

Anode-free sodium all-solid-state full cell

To demonstrate an anode-free sodium all-solid-state full cell, a low-cost $NaCrO_2$ cathode was used and paired with a $Na_{0.625}Y_{0.25}Zr_{0.75}Cl_{4.375}$ catholyte (Supplementary Fig. 15) that is known to be electrochemically stable against $NaCrO_2$ (ref. 55). When cycled at room temperature, the cell experienced noticeable polarization (Fig. 7a). To overcome the slow cathode kinetics, the full cell was cycled at a higher temperature of 40 °C (Fig. 7b). This improved the cathode capacity utilization at higher currents (Fig. 7c). Additionally, a constant voltage hold can be added at the charged state to maximize the extraction of capacity from the cathode. With this protocol, an ICE of 93% was achieved, which is similar to the ICE achieved in anode-free half cells (Fig. 7d). The cell maintained stable cycling for 400 cycles with a capacity retention of 70% (Fig. 7e), which is due to the high average Coulombic efficiency of 99.96% achieved under these cycling conditions (10 MPa, 40 °C). This performance is attributed to the combination of the aluminium pellet current collector with the sodium borohydride solid electrolyte. This

demonstrates the substantial improvement when using an aluminium pellet compared with conventional aluminium foil, which can only cycle for tens of cycles before losing most of its capacity (Fig. 7f). Although the aluminium pellet current collector used in this study is several hundred microns thick (Supplementary Fig. 16), reducing the thickness may be possible by using a thin layer of aluminium particles cast onto aluminium foil followed by a transfer process (Supplementary Fig. 17). Furthermore, although higher cathode loadings and thinner solid electrolyte layers will be needed to enable the full potential of this cell architecture, this truly anode-free cell design demonstrates the effectiveness of dense solid electrolyte and current collector morphologies and a robust interface between them.

Conclusions

In this work, we enable stable cycling in an anode-free all-solid-state battery architecture, which can potentially lead to a considerable increase in energy density. A pelletized aluminium current collector was shown to enable improved solid–solid interface contact with the borohydride-based solid electrolyte. This intimate interface enabled noticeably higher current density cycling. By pairing the dense aluminium pellet current collector with a sodium borohydride solid electrolyte, reversible cycling was achieved for capacities as high as 7 mAh cm^{-2} (62 µm of sodium) due to the electrochemically stable and dense solid electrolyte combined with the application of 10 MPa stack pressure. Using a low-cost $NaCrO_2$ cathode, an anode-free sodium all-solid-state full cell battery was demonstrated to cycle several hundred cycles. This work elucidates the four critical factors that govern the electrochemical performance of anode-free solid-state cell designs to guide future developments of high-energy all-solid-state batteries. We believe that this work can guide the discovery and implementation of other anode-free battery chemistries and serve as an example that sodium can compete with and complement traditional lithium-ion batteries.

Methods

Material synthesis

$NaCrO_2$. A stoichiometric amount of Na_2CO_3 (99.5%, Alfa Aesar) and Cr_2O_3 (99.97%, Alfa Aesar) was mixed with a mortar and pestle. This 1 g mixture was then pelletized under 370 MPa and then heated in a tube furnace under flowing argon at 5 °C min^{-1} to 900 °C and held for 10 h before ambient cooling to room temperature (~5 h). XRD data for the obtained material are shown in Supplementary Fig. 20.

Na_9Sn_4. A stoichiometric amount of Na metal (99.8%, Sigma Aldrich) and Sn powder (10 µm, 99%, Sigma Aldrich) was mixed with a mortar and pestle in an argon-filled glovebox. This 1 g mixture was then ball milled at 500 rpm for 2 h in a Retsch Emax high-energy ball mill in zirconia-lined airtight jars. XRD data for the obtained material are shown in Supplementary Fig. 21.

$Na_4B_{10}H_{10}B_{12}H_{12}$. A stoichiometric amount of $Na_2B_{10}H_{10}$ (Boron Specialties) and $Na_2B_{12}H_{12}$ (Boron Specialties) was mixed with a mortar and pestle in an argon-filled glovebox. This 1 g mixture was then ball milled at 450 rpm for 2 h in a Retsch PM100 planetary ball mill in zirconia-lined airtight jars. The resulting material was then dried at 175 °C for 48 h under dynamic vacuum. XRD data for the obtained material are shown in Supplementary Fig. 21, and conductivity measurements are shown in Supplementary Fig. 2.

$Na_{0.625}Y_{0.25}Zr_{0.75}Cl_{4.375}$. A stoichiometric amount of NaCl (99%, anhydrous, Sigma Aldrich), YCl_3 (99.99%, anhydrous, Sigma Aldrich) and $ZrCl_4$ (99.99%, anhydrous, Sigma Aldrich) were mixed with a mortar and pestle in an argon-filled glovebox. This 1 g mixture was then ball milled at 500 rpm for 2.5 h in a Retsch Emax high-energy ball mill in zirconia-lined airtight jars. The material was removed and homogenized with a mortar and pestle before ball milling for an additional 2.5 h. XRD data for the obtained material are shown in Supplementary Fig. 20, and conductivity measurements are shown in Supplementary Fig. 15.

Na_3PS_4. A stoichiometric amount of Na_2S (99%, anhydrous, Nagao) and P_2S_5 (99%, Sigma Aldrich) was mixed with a mortar and pestle in an argon-filled glovebox. This 1 g mixture was then ball milled at 450 rpm for 2 h in a Retsch PM100 planetary ball mill in zirconia-lined airtight jars.

$Li_4B_{10}H_{10}B_{12}H_{12}$. A stoichiometric amount of $Li_2B_{10}H_{10}$ (Boron Specialties) and $Li_2B_{12}H_{12}$ (Boron Specialties) was mixed with a mortar and pestle in an argon-filled glovebox. This 1 g mixture was then ball milled at 450 rpm for 2 h in a Retsch PM100 planetary ball mill in zirconia-lined airtight jars. The resulting material was then dried at 175 °C for 48 h under dynamic vacuum. The material was then ball milled again for 2 h.

Li_6PS_5Cl. Li_6PS_5Cl was obtained from NEI Corporation.

Li_7Sn_3. A stoichiometric amount of Stabilized Lithium Metal Powder metal (FMC) and Sn powder (10 µm, 99%, Sigma Aldrich) was mixed very gently with a mortar and pestle in an argon-filled glovebox. Note that the reaction becomes self-propagating during mixing.

Cathode composite fabrication

$NaCrO_2$, $Na_{0.625}Y_{0.25}Zr_{0.75}Cl_{4.375}$ (*a*-NYZC) and vapour-grown carbon fibres (98%, Sigma Aldrich) were mixed in a 11:16:1 weight ratio with a mortar and pestle.

Cell assembly

Fifty mg of NBH was pressed between two polished titanium plungers in a 10 mm diameter polyether ether ketone (PEEK) die at 100 MPa in an argon-filled glovebox.

Half cells. One hundred mg of Na_9Sn_4 was added to one side and 200 mg of Al powder (99.97%, −325 mesh; Fisher Scientific), Cu powder (99%, −325 mesh; Fisher Scientific) or Ti powder (93%, <20 µm; Fisher Scientific) was added to the other side of the NBH separator. The cells were then pressed at 370 MPa.

Full cells. Ten mg of *a*-NYZC was added as a protective layer between the NBH separator and the cathode composite. This *a*-NYZC layer was smoothed and pressed gently by hand with a Ti plunger. Then 24 mg of cathode composite was added on top of the *a*-NYZC layer. When using the Al pellet current collector, 200 mg of Al powder was then added to the other side of the NBH. When using Al foil, a 10 mm diameter circle of Al foil was added to the other side of the NBH. The cell was then pressed at 370 MPa.

Cell cycling

Cells were mounted in clamps containing a pressure sensor and springs to maintain a known and constant pressure during cycling. Unless otherwise noted, cells were cycled under 10 MPa constant pressure at room temperature.

Critical current density measurements. Various cells were evaluated by cycling various fixed capacities of sodium between the electrodes and the current density was increased stepwise after each cycle by 0.2 mA cm^{-2}. The critical current density was assessed to be the current density at which the cell exhibited short circuit behaviour (sudden drop and fluctuating of potential).

Capacity retention in half cells. A certain fixed capacity of sodium was plated onto the anode-free electrode. The sodium was then stripped away until a 2 V cut-off was reached. In the next cycle, the amount of sodium plating was set to the amount of sodium stripped during the

previous cycle. For example, if 1 mAh cm^{-2} was plated and 0.95 mAh cm^{-2} was able to be stripped, then in the next cycle 0.95 mAh cm^{-2} was plated. This was done to model the capacity retention of anode-free full cells, assuming that the cathode is 100% efficient.

Anode-free full cell. The anode-free full cell was cycled using 3.5 and 1.8 V upper and lower voltage cut-offs, respectively. Three formation cycles at 0.5 mA cm^{-2} were done before switching to 1 mA cm^{-2}. A constant voltage step was added to the end of the constant current charge step to obtain more capacity from the cathode due to cathode kinetic limitations within the sodium cathode composite. The constant voltage was held at 3.5 V until the current reached a value <0.2 mA cm^{-2}. Cycling was conducted at 40 °C at 10 MPa.

Electrochemical measurements

Electrochemical impedance spectroscopy. A Solartron 1260 impedance analyser was used for impedance measurements. A frequency range of 1 MHz to 1 Hz was used with an applied a.c. amplitude of 30 mV. To evaluate solid electrolyte ionic conductivity, 70 mg of solid electrolyte was pressed at 370 MPa between two titanium plungers in a 10 mm diameter PEEK die. Five mg of acetylene black carbon was added to each side of the electrolyte pellet, and the cell was pressed again at 370 MPa. Carbon was added to improve the physical contact between the sample and the electrodes to minimize the interface resistance and obtain a more accurate electrolyte conductivity value.

Direct current polarization. The same cell configuration used for EIS measurements was used for electronic conductivity measurements. A 50 mV potential was applied to the cell and the current response was measured as a function of time. The current value after 300 s was used to calculate the electronic conductivity of the solid electrolytes.

Linear sweep voltammetry. Nine mg of solid electrolyte and 21 mg of stainless-steel powder was mixed with a mortar and pestle. Seventy mg of solid electrolyte was pressed at 370 MPa between two titanium plungers in a 10 mm diameter PEEK die. Fifty mg of Na_9Sn_4 was added to one side of the solid electrolyte and 20 mg of the solid electrolyte/steel mixture was added to the other side. The cell was pressed again at 370 MPa. Two cells were fabricated for each solid electrolyte. One cell was swept to low potential and the other cell was swept to high potential at a rate of 0.1 mV s^{-1}.

Optical profilometry

A Filmetrics Profilm3D Optical Profiler was used for measurements. A 50× objective lens, white light interferometry, an envelope peak/centre setting and 30 µm scan length were used. Data were analysed using the profilmonline web-based software.

Focused-ion beam scanning electron microscopy

Ga^+ ion source. An FEI Scios Dualbeam FIB/SEM was used. Sample milling was conducted at 30 kV with a 65 nA current. After the initial removal of material, a lower current (7 nA) was used to clean the cross-section surface. Electron imaging was conducted at 5 kV and 0.1 nA beam conditions. An airtight transfer arm was used to avoid sample exposure to air. The Ga^+ source machine was used for Figs. 3c and 6f,g and Supplementary Figs. 8, 14 and 17. For sodium metal milling, a liquid nitrogen cooled cryogenic stage was used. For EDS mapping of boron as shown in Supplementary Fig. 14, an 'AP3' polymer detector window was used as part of the Bruker XFlash 6|60 EDS system. This window type enables the detection of light elements such as boron.

Xe^+ plasma source. A Helios G4 PFIB UXe DualBeam FIB/SEM was used. Sample milling was conducted at 30 kV with a 2.5 µA current. After the initial removal of material, lower currents (500 and 60 nA) were used to clean the cross-section surface. Electron imaging was conducted at 5 kV and 0.4 nA beam conditions. The Xe^+ source machine was used for the Al, Cu and Ti current collector samples in Fig. 5.

Scanning and transmission electron microscopy

Transmission electron microscopy (TEM) images of Al, Cu and Ti particle surfaces were obtained using a Thermofisher Talos F200X G2, equipped with a Ceta camera and operated at 200 kV. Scanning/TEM-energy dispersive X-ray spectroscopy data was obtained using 4-in-column Super-X silicon drift detectors.

X-ray photoelectron spectroscopy

A Kratos Axis Supra instrument utilizing Al kα radiation was used for XPS measurements. The sample chamber pressure was $<5 \times 10^{-8}$ Torr. A dwell time of 100 ms, 0.1 eV scan resolution and a charge neutralizer was used for measurements. Etching was conducted using argon plasma at time intervals of 5 min to probe the chemical composition of the sample surface as a function of depth. Data analysis was performed using CasaXPS software and the carbon 1 s peak was used for calibration. A Shirley-type background was used.

X-ray diffraction

A Bruker APEX II Ultra diffractometer was used for diffraction measurements. A molybdenum X-ray source (Kα-λ = 0.7093 Å) was used at 40 kV and 40 mA. Flame-sealed boron-rich glass capillaries were used due to the air sensitivity of the materials. A 2D detector collected the diffraction data and 2D patterns were produced by merging and integrating the data with DIFFRAC.EVA (Bruker, 2018). Rietveld refinement was performed using the FullProf software suite. XRD data for plated sodium were obtained by delaminating a half cell and sealing the surface of the exposed sodium with Kapton tape before obtaining the measurement using a Rigaku Miniflex diffractometer with Cu radiation.

X-ray computed tomography

A 4-mm-diameter cell design was used for computed tomography measurements. A half-cell configuration (Na_9Sn_4-NBH-Al) was used. Using a Versa 510 (Zeiss/Xradia) X-ray microscope, a 360° scan was obtained. A 10 s exposure setting, 80 kV source voltage and 7 W power were used for the measurements with the objective of 4× without additional filter. The field of view of 2.24 mm × 2.24 mm with a voxel size of 2.22 µm was achieved. Amira 2019.1 software was used for data reconstruction.

Scanning electron microscopy

SEM micrographs were obtained with a FEI Apreo instrument. A 5 keV accelerating voltage, 0.1 nA current and Everhart–Thornley detector were used.

Data availability

All data generated or analysed during the current study are included in this article and its Supplementary Information file.

References

1. Nishi, Y. The dawn of lithium-ion batteries. *Electrochem. Soc. Interface* **25**, 71–74 (2016).
2. Hirsh, H. S. et al. Sodium-ion batteries paving the way for grid energy storage. *Adv. Energy Mater.* **10**, 2001274 (2020).
3. Qian, J. et al. Anode-free rechargeable lithium metal batteries. *Adv. Funct. Mater.* **26**, 7094–7102 (2016).
4. Fang, C. et al. Quantifying inactive lithium in lithium metal batteries. *Nature* **572**, 511–515 (2019).
5. Tang, S. et al. A room-temperature sodium metal anode enabled by a sodiophilic layer. *Nano Energy* **48**, 101–106 (2018).
6. Wu, H., Jia, H., Wang, C., Zhang, J.-G. & Xu, W. Recent progress in understanding solid electrolyte interphase on lithium metal anodes. *Adv. Energy Mater.* **11**, 2003092 (2021).

7. Matios, E., Wang, H., Wang, C. & Li, W. Enabling safe sodium metal batteries by solid electrolyte interphase engineering: a review. *Ind. Eng. Chem. Res.* **58**, 9758–9780 (2019).
8. Zhang, Z. et al. Capturing the swelling of solid-electrolyte interphase in lithium metal batteries. *Science* **375**, 66–70 (2022).
9. Gao, L., Chen, J., Chen, Q. & Kong, X. The chemical evolution of solid electrolyte interface in sodium metal batteries. *Sci. Adv.* **8**, eabm4606 (2022).
10. Wang, Y. et al. Developments and perspectives on emerging high-energy-density sodium-metal batteries. *Chem* **5**, 2547–2570 (2019).
11. Lu, Z., Yang, H., Yang, Q.-H., He, P. & Zhou, H. Building a beyond concentrated electrolyte for high-voltage anode-free rechargeable sodium batteries. *Angew. Chem. Int. Ed.* **61**, e202200410 (2022).
12. Mao, M. et al. Anion-enrichment interface enables high-voltage anode-free lithium metal batteries. *Nat. Commun.* **14**, 1082 (2023).
13. Su, L., Charalambous, H., Cui, Z. & Manthiram, A. High-efficiency, anode-free lithium–metal batteries with a close-packed homogeneous lithium morphology. *Energy Environ. Sci.* **15**, 843–854 (2022).
14. Lin, C.-C. et al. Nanotwinned copper foil for 'zero excess' lithium–metal batteries. *ACS Appl. Energy Mater.* **6**, 2140–2150 (2023).
15. Louli, A. J. et al. Exploring the impact of mechanical pressure on the performance of anode-free lithium metal cells. *J. Electrochem. Soc.* **166**, A1291 (2019).
16. Shin, W. & Manthiram, A. A facile potential hold method for fostering an inorganic solid-electrolyte interphase for anode-free lithium-metal batteries. *Angew. Chem. Int. Ed.* **61**, e202115909 (2022).
17. Spencer Jolly, D. et al. Sodium/Na β″ alumina interface: effect of pressure on voids. *ACS Appl. Mater. Interfaces* **12**, 678–685 (2020).
18. Bates, J. B., Dudney, N. J., Neudecker, B., Ueda, A. & Evans, C. D. Thin-film lithium and lithium-ion batteries. *Solid State Ion.* **135**, 33–45 (2000).
19. Neudecker, B. J., Dudney, N. J. & Bates, J. B. 'Lithium-free' thin-film battery with in situ plated Li anode. *J. Electrochem. Soc.* **147**, 517 (2000).
20. Wang, M. J., Carmona, E., Gupta, A., Albertus, P. & Sakamoto, J. Enabling 'lithium-free' manufacturing of pure lithium metal solid-state batteries through in situ plating. *Nat. Commun.* **11**, 5201 (2020).
21. Gu, D., Kim, H., Lee, J.-H. & Park, S. Surface-roughened current collectors for anode-free all-solid-state batteries. *J. Energy Chem.* **70**, 248–257 (2022).
22. Lee, D. et al. Sacrificial cathode additives for enhanced cycle performance for liquid and all-solid-state anode-free lithium secondary batteries. *J. Alloys Compd.* **950**, 169910 (2023).
23. Lewis, J. A. et al. Accelerated short circuiting in anode-free solid-state batteries driven by local lithium depletion. *Adv. Energy Mater.* **13**, 2204186 (2023).
24. Lee, Y.-G. et al. High-energy long-cycling all-solid-state lithium metal batteries enabled by silver–carbon composite anodes. *Nat. Energy* **5**, 299–308 (2020).
25. Gu, D., Kim, H., Kim, B.-K., Lee, J.-H. & Park, S. Chlorine-rich lithium argyrodite enables stable interfacial Li plating/stripping behavior in anode-free all-solid-state batteries. *CrystEngComm* **25**, 4182–4188 (2023).
26. Ortmann, T. et al. Deposition of sodium metal at the copper-NaSICON interface for reservoir-free solid-state sodium batteries. *Adv. Energy Mater.* **14**, 2302729 (2024).
27. Heubner, C. et al. From lithium-metal toward anode-free solid-state batteries: current developments, issues, and challenges. *Adv. Funct. Mater.* **31**, 2106608 (2021).
28. Shen, F., Dixit, M. B., Xiao, X. & Hatzell, K. B. Effect of pore connectivity on Li dendrite propagation within LLZO electrolytes observed with synchrotron X-ray tomography. *ACS Energy Lett.* **3**, 1056–1061 (2018).
29. Kazyak, E. et al. Li penetration in ceramic solid electrolytes: operando microscopy analysis of morphology, propagation, and reversibility. *Matter* **2**, 1025–1048 (2020).
30. Luo, S. et al. Growth of lithium-indium dendrites in all-solid-state lithium-based batteries with sulfide electrolytes. *Nat. Commun.* **12**, 6968 (2021).
31. Yuan, C. et al. Coupled crack propagation and dendrite growth in solid electrolyte of all-solid-state battery. *Nano Energy* **86**, 106057 (2021).
32. Liu, S. et al. Porous Al current collector for dendrite-free Na metal anodes. *Nano Lett.* **17**, 5862–5868 (2017).
33. Yun, Q. et al. Chemical dealloying derived 3D porous current collector for Li metal anodes. *Adv. Mater.* **28**, 6932–6939 (2016).
34. Deysher, G. et al. Evaluating electrolyte–anode interface stability in sodium all-solid-state batteries. *ACS Appl. Mater. Interfaces* **14**, 47706–47715 (2022).
35. Duchêne, L. et al. A highly stable sodium solid-state electrolyte based on a dodeca/deca-borate equimolar mixture. *Chem. Commun.* **53**, 4195–4198 (2017).
36. Wang, M. J., Chang, J.-Y., Wolfenstine, J. B. & Sakamoto, J. Analysis of elastic, plastic, and creep properties of sodium metal and implications for solid-state batteries. *Materialia* **12**, 100792 (2020).
37. Orsini, F. et al. In situ scanning electron microscopy (SEM) observation of interfaces within plastic lithium batteries. *J. Power Sources* **76**, 19–29 (1998).
38. Orsini, F. et al. In situ SEM study of the interfaces in plastic lithium cells. *J. Power Sources* **81–82**, 918–921 (1999).
39. Seong, I. W., Hong, C. H., Kim, B. K. & Yoon, W. Y. The effects of current density and amount of discharge on dendrite formation in the lithium powder anode electrode. *J. Power Sources* **178**, 769–773 (2008).
40. Zhou, C. et al. Polymorphism, ionic conductivity and electrochemical properties of lithium closo-deca- and dodeca-borates and their composites, $Li_2B_{10}H_{10}$–$Li_2B_{12}H_{12}$. *J. Mater. Chem. A* **10**, 16137–16151 (2022).
41. Barai, P. et al. The role of local inhomogeneities on dendrite growth in LLZO-based solid electrolytes. *J. Electrochem. Soc.* **167**, 100537 (2020).
42. Lu, Z. & Ciucci, F. Metal borohydrides as electrolytes for solid-state Li, Na, Mg, and Ca batteries: a first-principles study. *Chem. Mater.* **29**, 9308–9319 (2017).
43. Murray, J. L. The Al–Na (aluminum–sodium) system. *Bull. Alloy Phase Diagr.* **4**, 407–410 (1983).
44. Pelton, A. D. The Cu–Na (copper–sodium) system. *Bull. Alloy Phase Diagr.* **7**, 25–27 (1986).
45. Bale, C. W. The Na–Ti (sodium–titanium) system. *Bull. Alloy Phase Diagr.* **10**, 138–139 (1989).
46. Samsonov, G. V. *Handbook of the Physicochemical Properties of the Elements* (Springer Science & Business Media, 2012).
47. Tan, D. H. S. et al. Carbon-free high-loading silicon anodes enabled by sulfide solid electrolytes. *Science* **373**, 1494–1499 (2021).
48. Randau, S. et al. Benchmarking the performance of all-solid-state lithium batteries. *Nat. Energy* **5**, 259–270 (2020).
49. Zhou, L. et al. High areal capacity, long cycle life 4V ceramic all-solid-state Li-ion batteries enabled by chloride solid electrolytes. *Nat. Energy* **7**, 83–93 (2022).
50. Zhou, L. et al. A new halospinel superionic conductor for high-voltage all solid state lithium batteries. *Energy Environ. Sci.* **13**, 2056–2063 (2020).

51. Zhou, L., Assoud, A., Zhang, Q., Wu, X. & Nazar, L. F. New family of argyrodite hioantimonate lithium superionic conductors. *J. Am. Chem. Soc.* **141**, 19002–19013 (2019).
52. Ham, S.-Y. et al. Assessing the critical current density of all-solid-state Li metal symmetric and full cells. *Energy Storage Mater.* **55**, 455–462 (2023).
53. Doux, J. M. et al. Stack pressure considerations for room-temperature all-solid-state lithium metal batteries. *Adv. Energy Mater.* **10**, 1903253 (2020).
54. LePage, W. S., Chen, Y., Poli, A., Thouless, M. D. & Dasgupta, N. P. Sodium mechanics: effects of temperature, strain rate, and grain rotation and implications for sodium metal batteries. *Extreme Mech. Lett.* **52**, 101644 (2022).
55. Ridley, P. et al. Amorphous and nanocrystalline halide solid electrolytes with enhanced sodium-ion conductivity. *Matter* **7**, 485–499 (2024).
56. Schlenker, R. et al. Understanding the lifetime of battery cells based on solid-state Li_6PS_5Cl electrolyte paired with lithium metal electrode. *ACS Appl. Mater. Interfaces* **12**, 20012–20025 (2020).
57. Yang, Z. et al. Developing a high-voltage electrolyte based on conjuncto-hydroborates for solid-state sodium batteries. *J. Mater. Chem. A* **10**, 7186–7194 (2022).
58. Jin, M., Yang, Z., Cheng, S. & Guo, Y. Fast sodium-ion conduction in a novel conjuncto-hydroborate of $Na_4B_{20}H_{18}$. *ACS Appl. Energy Mater.* **5**, 15578–15585 (2022).
59. Kasemchainan, J. et al. Critical stripping current leads to dendrite formation on plating in lithium anode solid electrolyte cells. *Nat. Mater.* **18**, 1105–1111 (2019).
60. Su, Y. et al. A more stable lithium anode by mechanical constriction for solid state batteries. *Energy Environ. Sci.* **13**, 908–916 (2020).
61. Bonnick, P. et al. A high performance all solid state lithium sulfur battery with lithium thiophosphate solid electrolyte. *J. Mater. Chem. A* **7**, 24173–24179 (2019).
62. Fan, X. et al. Fluorinated solid electrolyte interphase enables highly reversible solid-state Li metal battery. *Sci. Adv.* **4**, eaau9245 (2018).
63. Liang, J. et al. An air-stable and dendrite-free Li anode for highly stable all-solid-state sulfide-based Li batteries. *Adv. Energy Mater.* **9**, 1902125 (2019).
64. Zhang, Z. et al. All-in-one improvement toward Li_6PS_5Br-based solid electrolytes triggered by compositional tune. *J. Power Sources* **410–411**, 162–170 (2019).
65. Garcia-Mendez, R., Mizuno, F., Zhang, R., Arthur, T. S. & Sakamoto, J. Effect of processing conditions of $75Li_2S$-25P2S5 solid electrolyte on its DC electrochemical behavior. *Electrochim. Acta* **237**, 144–151 (2017).
66. Zhang, Z. et al. One-step solution process toward formation of Li_6PS_5Cl argyrodite solid electrolyte for all-solid-state lithium-ion batteries. *J. Alloys Compd.* **812**, 152103 (2020).
67. Pang, B. et al. Ag nanoparticles incorporated interlayer enables ultrahigh critical current density for Li_6PS_5Cl-based all-solid-state lithium batteries. *J. Power Sources* **563**, 232836 (2023).
68. Wu, M. et al. In situ formed LiF-Li_3N interface layer enables ultra-stable sulfide electrolyte-based all-solid-state lithium batteries. *J. Energy Chem.* **79**, 272–278 (2023).
69. Subramanian, Y., Rajagopal, R., Kang, S. & Ryu, K.-S. Enhancement of lithium argyrodite interface stability through MoO_2 substitution and its application in lithium solid state batteries. *J. Alloys Compd.* **925**, 166596 (2022).
70. Zou, C. et al. $LiAlO_2$-coated $LiNi_{0.8}Co_{0.1}Mn_{0.1}O_2$ and chlorine-rich argyrodite enabling high-performance all-solid-state lithium batteries at suitable stack pressure. *Ceram. Int.* **49**, 443–449 (2023).
71. Subramanian, Y., Rajagopal, R. & Ryu, K.-S. Blending a Li_3N/Li_3YCl_6 solid electrolyte with Li_6PS_5Cl argyrodite structure to improve interface stability and electrochemical performance in lithium solid-state batteries. *J. Alloys Compd.* **940**, 168867 (2023).
72. Liu, Y. et al. Revealing the impact of Cl substitution on the crystallization behavior and interfacial stability of superionic lithium argyrodites. *Adv. Funct. Mater.* **32**, 2207978 (2022).
73. Lewis, J. A. et al. Role of areal capacity in determining short circuiting of sulfide-based solid-state batteries. *ACS Appl. Mater. Interfaces* **14**, 4051–4060 (2022).
74. Wang, G. et al. Hydrolysis-resistant and anti-dendritic halide composite Li_3PS_4-LiI solid electrolyte for all-solid-state lithium batteries. *Electrochim. Acta* **428**, 140906 (2022).
75. Zhao, B. et al. Stabilizing $Li_7P_3S_{11}$/lithium metal anode interface by in-situ bifunctional composite layer. *Chem. Eng. J.* **429**, 132411 (2022).
76. Wu, M., Liu, G. & Yao, X. Oxygen doped argyrodite electrolyte for all-solid-state lithium batteries. *Appl. Phys. Lett.* **121**, 203904 (2022).
77. Kim, H.-M., Subramanian, Y. & Ryu, K.-S. Improved electrochemical and air stability performance of SeS_2 doped argyrodite lithium superionic conductors for all-solid-state lithium batteries. *Electrochim. Acta* **442**, 141869 (2023).
78. Ni, Y., Huang, C., Liu, H., Liang, Y. & Fan, L.-Z. A high air-stability and Li-metal-compatible $Li_{3+2x}P_{1-x}Bi_xS_{4-1.5x}O_{1.5x}$ sulfide electrolyte for all-solid-state Li–metal batteries. *Adv. Funct. Mater.* **32**, 2205998 (2022).

Acknowledgements

Funding to support this work was provided by the National Science Foundation through the Partnerships for Innovation (PFI) grant number 2044465 received by Y.S.M. This work was performed in part at the San Diego Nanotechnology Infrastructure (SDNI) of UCSD, a member of the National Nanotechnology Coordinated Infrastructure, which is supported by the National Science Foundation (grant ECCS-2025752). We acknowledge the use of facilities and instrumentation at the UC Irvine Materials Research Institute (IMRI), which is supported in part by the National Science Foundation through the UC Irvine Materials Research Science and Engineering Center (DMR-2011967). Specifically, the XPS work was performed using instrumentation funded in part by the National Science Foundation Major Research Instrumentation Program under grant number CHE-1338173. Xe plasma FIB experiments were conducted at the University of Southern California in the Core Center of Excellence in Nano Imaging. We also acknowledge the use of the UCSD Crystallography Facility.

Author contributions

G.D., J.J. and Y.S.M. conceived the ideas. G.D. and J.J. designed the cell architecture and electrochemical measurements, which were performed by G.D. G.D. performed optical profilometry experiments. Y-T.C. collected plasma FIB images, and G.D. and S-Y.H. collected gallium FIB data. S-Y.H. performed X-ray CT experiments. B.S. and K.Q. collected the XRD data. D.C. performed the TEM imaging experiments. G.D. wrote the manuscript. J.J., J.A.S.O, L.H.B.N., P.R., A.C. and S.W.-H.L. participated in the scientific discussion and helped edit the manuscript. Discussion of the results included all authors. All authors have provided input on and have approved the final manuscript.

Competing interests

A provisional patent application (US Provisional Application serial number 63590739) for this work has been filed by G.D. and Y.S.M. through UC San Diego's Office of Innovation and Commercialization. This patent application contains claims related to the use of aluminium particles pressed into an NBH electrolyte separator for use as a current collector in an anode-free battery. The remaining authors declare no competing interests.

Additional information

Supplementary information The online version contains supplementary material available at https://doi.org/10.1038/s41560-024-01569-9.

Correspondence and requests for materials should be addressed to Jihyun Jang or Ying Shirley Meng.

Peer review information *Nature Energy* thanks Sangbaek Park and the other, anonymous, reviewer(s) for their contribution to the peer review of this work.